Influence of the ionic size on the evolution of local Jahn-Teller distortions in cobaltites

D. Phelan,[1] Despina Louca,[1] K. Kamazawa,[1] M. F. Hundley,[2] and K. Yamada[3]
[1]*Department of Physics, University of Virginia, Charlottesville, Virginia 22904, USA*
[2]*Los Alamos National Laboratory, Los Alamos, New Mexico 87454, USA*
[3]*Institute of Materials Research, Tohoku University, Sendai 980-8577, Japan*
(Received 10 May 2007; revised manuscript received 2 August 2007; published 20 September 2007)

The thermodynamic and atomic structure properties of $La_{1-x}A_xCoO_3$ ($A=Ba^{2+}$ and Ca^{2+}) with $0 \leqslant x \leqslant 0.5$, a class of compounds that exhibit magnetoresistance in the presence of an applied magnetic field, have been investigated via magnetic and transport measurements and neutron scattering. While in the parent compound, the Co^{3+} ion undergoes a spin-state transition from the low-spin ground state to a dynamic intermediate-spin configuration *thermally*, with hole doping, the intermediate-spin state becomes static as evidenced by the Jahn-Teller octahedral splitting of the Co-O bonds. The size of the split depends strongly on the tolerance factor, where small or no Jahn-Teller distortions are observed in samples with small tolerance factors (i.e., Ca), but as the tolerance factor approaches 1 (i.e., Ba), the bond split can be as much as 0.2 Å. At the same time, ferromagnetic ordering is also influenced by the tolerance factor. As it gets closer to 1, ferromagnetic coupling is enhanced due to the straightening of the Co-O-Co bonds, where the angle becomes almost 180° that, in turn, favors double-exchange interactions between Co ions. With the ferromagnetic transition, the system becomes metallic and shows a negative magnetoresistance with field. As the tolerance factor is reduced from 1, the ferromagnetic coupling is weak and the bond angle is about 160°.

DOI: 10.1103/PhysRevB.76.104111 PACS number(s): 61.12.−q, 71.70.−d, 71.30.+h

I. INTRODUCTION

The unusual properties displayed by transition metal perovskite oxides are largely a manifestation of intricate electron correlation effects that govern most of their physical functions. In particular, the class of perovskites that display large field-induced magnetoresistance (MR) in the presence of an applied external field is governed by competing interactions between tendencies for strong localization via polaron formation and metallic itineracy[1] that lead to phenomena such as phase separation and charge and/or spin stripe formation. The effects pertaining to the MR perovskites are not uncommon in nature as they have been observed in other strongly correlated electron systems such as cuprates and nickelates with direct implications to superconductivity.[2] The perovskite cobaltites offer a venue to study many of the intricate properties displayed by complex oxides. Compounds such as $La_{1-x}A_xCoO_3$, where A^{2+} is a divalent cation such as Ca, Ba, or Sr, are particularly interesting because of the complexity that originates from the nearly degenerate spin-state configurations that can occur in the Co^{3+} ion. It has been known for several decades that the ground state of the Co^{3+} in the parent compound is the nonmagnetic low spin (LS), $S=0$, $t_{2g}^6 e_g^0$ state, and that a transition to paramagnetic behavior upon warming (around 100 K) is caused by the thermal excitation of magnetic spin states.[3–8] A number of studies have debated whether the thermally activated state is the intermediate spin (IS), $S=1$, $t_{2g}^5 e_g^1$ configuration, or high spin (HS), $S=2$, $t_{2g}^4 e_g^2$ configuration, and a plethora of reports have appeared in the literature recently, supporting one scheme or another, making this a hotly debated issue.[9–32] As the hole concentration is increased from $x>0$, the insulating, nonmagnetic ground state of the parent gives way to a metallic, ferromagnetic-like state.[3,33–42] This behavior is reminiscent of manganites,[43,44] except that the parent compound in manganites is an *antiferromagnetic* insulator and the spin states of $Mn^{3+/4+}$ are well known, whereas the evolution of the Co^{3+} spin states with doping is not well understood.

The addition of holes into $LaCoO_3$ through the substitution of a divalent ion for La^{3+} introduces Co^{4+} ions into the lattice, and these are anticipated to acquire a LS, $S=\frac{1}{2}$, configuration. Short-range ferromagnetic correlations develop with low doping in $La_{1-x}A_xCoO_3$,[8] and a phase transition to a ferromagnetic cluster glass at $x\sim0.18$ when $A=Sr$,[36] $x\sim0.20$ when $A=Ba$,[41] and possibly as low as $x\sim0.05$ when $A=Ca$.[41] This magnetic transition is coincident with an insulator-metal transition for $A=Sr$ and Ba, while in the case of Ca, it appears to occur for $x>0.2$ based on the data of Ref. 41. The addition of charge carriers induces a magnetic moment on the surrounding Co^{3+} ions that changes their electronic configuration. It has been argued that the $S=1$ spin state is stabilized on the six Co^{3+} ions surrounding a Co^{4+} ion, thus forming a seven-site magnetopolaron in $La_{1-x}Sr_xCoO_3$,[45,46] and that the transition to a metallic ferromagnet results from the percolation of hole-rich ferromagnetic clusters driven by double-exchange coupling between IS Co^{3+} and LS Co^{4+}.[28] Yet, the presence of IS Co^{3+} in the doped compounds remains controversial as it has been recently argued that HS Co^{3+} is instead stabilized,[32] and the mechanism by which either IS or HS is stabilized remains unclear. At the same time, the extent to which the stabilization of one state over the other is dependent on structural changes that occur when La^{3+} is replaced by a differently sized ion has not been investigated, and this is the focus of the present paper. In the parent compound, the energy levels of the $S=0$ state and the first excited state are determined by the competition of the crystal field splitting, intra-atomic magnetic exchange interactions, and the e_g-$2p$ hybridization. It is reasonable to expect than when La^{3+} ions are replaced by a divalent dopant, changes that occur in the lattice will

affect the relative strengths of the competing energies, i.e., subtle lattice expansion or contraction will change the strength of the octahedral crystal field as well as the e_g-O_{2p} hybridization. To address the role of the lattice, we can compare the effects of doping with divalent ions of different sizes. Electronically, the hole concentration can be increased in the same way by the substitution of Ca^{2+}, Sr^{2+}, or Ba^{2+} for La^{3+} (hereafter, we refer to these series as LCCO, LSCO, and LBCO). However, the dopants differ significantly in their nominal ionic radii of 1.18, 1.31, and 1.47 Å in the IX coordination, respectively,[47] while the nominal radius of La^{3+} is 1.216 Å. This changes the tolerance factor and introduces steric effects with important implications in the elastic energy and electron-lattice interactions.

Experimentally, an approach for carrying out an investigation of the role of the lattice on the spin-state transition is a close examination of the structure. This is because the IS state ($t_{2g}^5 e_g^1$) has orbital e_g degeneracy, making it Jahn-Teller (JT) active; therefore, it is expected that the octahedral Co-O environment will distort in an effort to relieve the orbital degeneracy. As an example, a similar e_g orbital degeneracy of Mn^{3+} ($t_{2g}^3 e_g^1$) ions in $LaMnO_3$ is relieved by a cooperative distortion of the octahedra, and an orthorhombic or monoclinic lowering of symmetry occurs.[48] HS and LS Co^{3+} lack e_g degeneracy and are not JT active. Thus, the observation of JT splitting in the cobaltite represents a signature of the IS state. However, a number of diffraction studies have failed to observe cooperative JT distortions in the average crystal structure in $LaCoO_3$, LSCO, or LCCO.[49–53] For instance, powder diffraction measurements of the parent compound, $LaCoO_3$, have been reported in which the structure was refined using rhombohedral ($R\bar{3}c$) symmetry.[49] In this symmetry, all octahedral Co-O bond lengths have the same distance, so no cooperative JT distortion is allowed. Recently, a single-crystal x-ray diffraction study of the parent compound[20] has suggested that a monoclinic phase resulting from cooperative orbital ordering may occur in $LaCoO_3$. Likewise, it has been reported that LSCO has $R\bar{3}c$ symmetry for all temperatures, at least up to a doping level of 50%.[51,52] LCCO, on the other hand, undergoes a low-temperature phase transition to orthorhombic symmetry[41,53] (*Pnma*), but this transition has been argued to have a steric origin. Only one study of powder diffraction has reported JT distortions in the average crystal structure for these cobaltites: the evidence was provided by the observation of a tetragonal ($P4/mmm$) lowering of symmetry in LBCO for $x=0.5$.[54] It is important to note that although no evidence for JT distortions has been observed in the average crystal structure, the local atomic structure is a better tool to investigate JT distortions that are not periodic in nature. The local atomic structure cannot be obtained by usual Rietveld refinement of powder diffraction data, but it can be determined by techniques such as the pair density function (PDF) analysis of pulsed neutron diffraction data or extended x-ray absorption fine structure (EXAFS). Reports of both PDF[14,45] and EXAFS[55] measurements on $LaCoO_3$ have identified local distortions of the Co-O environment from that predicted by $R\bar{3}c$ symmetry above the thermal spin-state transition temperature, which have been interpreted as evidence for IS Co^{3+}. Likewise, JT distortions were identified by PDF analysis in LSCO,[14,45] and by considering the peak splitting, the concentration of JT active ions was estimated as a function of the hole concentration. One of the major goals of the current work is to determine the dependence of the JT effect on the ionic size in the LCCO and LBCO series in an effort to understand how the lattice couples with the magnetic and transport transitions.

In this paper, we report the results of measurements of the magnetic, transport, and structural properties of LCCO and LBCO in an attempt to determine the role of the structure on the stabilization of the IS state and on the evolution of the nonmagnetic, insulating parent into an itinerant ferromagnet. We find that as the lattice expands and Co-O-Co bonds approach 180° in the *average* structure, a split develops in the Co-O bonds in the *local* atomic structure as a function of temperature, suggesting that the expansion of the lattice and straightening of bonds promote the stabilization of the IS state. The rest of the paper is organized as follows. In Sec. II, the synthesis of powder samples and the details of our magnetization and neutron diffraction measurements are described. In Sec. III A, the measurements of the magnetization of LCCO and LBCO are discussed. In Sec. III B, the ferromagnetic reflections from neutron diffraction are compared as a function of concentration in LCCO and LBCO. We show that a weak reflection appears at a lower concentration in LCCO than in LBCO, but that the intensity of the reflections in LCCO saturates with a much weaker strength than in LBCO and at a smaller doping concentration. In Sec. III C, we report the results of Rietveld refinement of the average crystal structure of LCCO and LBCO. Due to the significant lattice expansion observed in LBCO, the crystal structure approaches the cubic aristotype at large x, whereas a lowering of the crystal symmetry to orthorhombic is observed in LCCO. In Sec. III D, the local structures of LCCO and LBCO are analyzed. A splitting of the Co-O bond lengths is observed as the temperature is increased, which we interpret as a signature of the presence of JT active, IS Co^{3+} ions. Based on the peak splitting, the fractions of Co ions that become JT active are estimated as a function of temperature and concentration. We argue that a higher fraction of JT active ions exists in LBCO than in LCCO, which is, in turn, related to the straightening of the Co-O-Co bonds and expansion of the lattice. Finally, the results are summarized in Sec. IV.

II. DETAILS OF EXPERIMENT AND ANALYSIS

Polycrystalline LCCO and LBCO were prepared by solid-state reaction, using a procedure similar to the one detailed in Ref. 41. The proper quantities of Co_3O_4, La_2O_3, and $CaCO_3$ or $BaCO_3$ were ground together, pressed into a pellet, and annealed at 850 °C in an alumina crucible for approximately two days. Next, the pellet was cooled to room temperature, crushed and ground, re-pressed into a new pellet, and annealed at 1200 °C in an alumina crucible for approximately two more days. As needed (generally two to three times), the pellet was again cooled, ground, re-pressed, and annealed at 1200 °C. The last annealing at 1200 °C was done in a controlled oxygen flow.

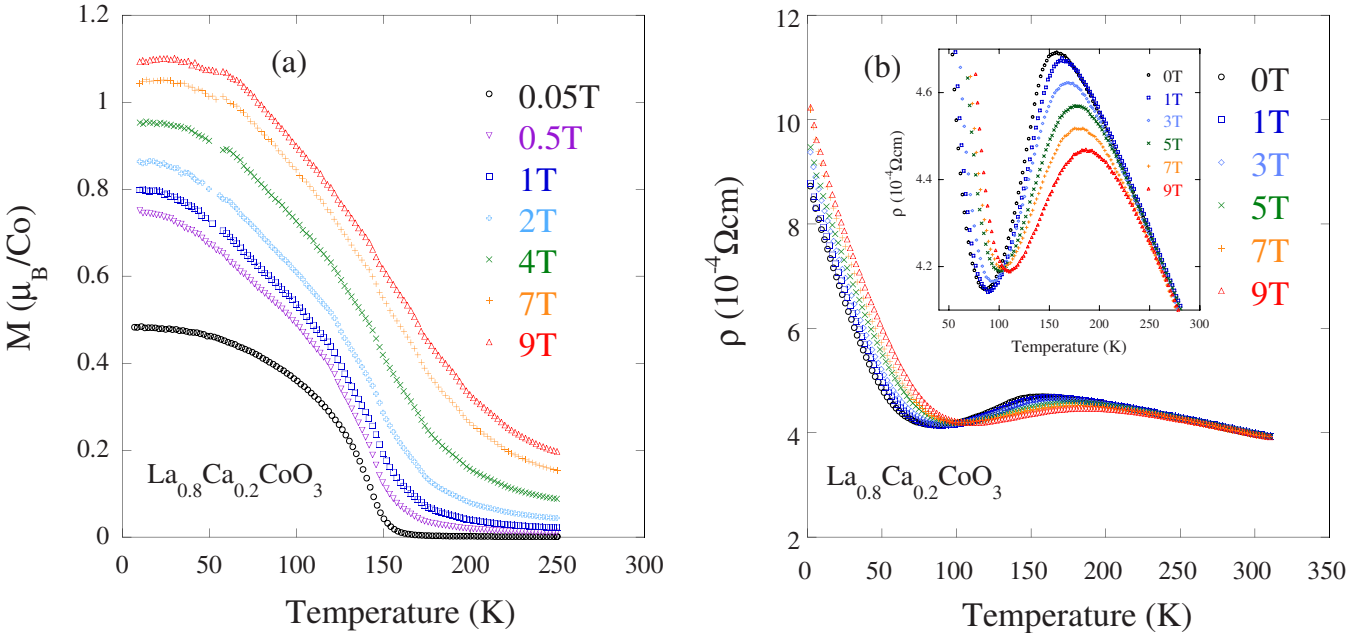

FIG. 1. (Color online) Magnetization and resistivity measurements for $La_{0.8}Ca_{0.2}CoO_3$. In (a), the magnetization is shown for different values of magnetic field as a function of temperature. It is evident that a ferromagnetic transition occurs at $T_c \sim 150$ K. The temperature at which the magnetization rises tends to increase with applied field. In (b), the resistivity is plotted for different values of magnetic field as a function of temperature. A broad hump is observed at T_c, and it is clear that the maximum of the hump shifts to higher temperature as the field is increased. As the temperature is decreased below ~100 K, the resistivity increases, indicating insulating behavior. The temperature at which the increase occurs is also dependent on the applied magnetic field.

The above preparation procedure worked well to make single-phase samples of LCCO for $x \leqslant 0.20$. For $x > 0.20$, a very weak (at least for $x \leqslant .30$) secondary phase emerged, which could not be identified; it was not one of the original starting materials. This agrees with the report of Ref. 53 in which a single-phase powder with $x > 0.20$ could not be synthesized and that of Ref. 56 in which samples with $x = 0.40$ and 0.50 had to be made by a citrate-gel method rather than solid-state reaction. For our purpose, the secondary phase is much smaller than the majority perovskite phase for $x = 0.30$ (less than 5%). Magnetization measurements were made in dc mode using the ACMS option of a Quantum Design Physical Property Measurement System. dc resistivity measurements were made using a standard four-probe technique on very thin, sintered powder pellets.

A single crystal of $La_{0.95}Ca_{0.05}CoO_3$ was grown using the floating-zone technique. Elastic single-crystal neutron scattering measurements were made at the SPINS cold-neutron triple-axis spectrometer at the NIST Center for Neutron Research using a 3.6 meV neutron energy, 80′-80′ collimation, and three flat pyrolytic graphite blades as an analyzer. A Be filter was placed before the sample and a BeO filter was placed after the sample. The crystal symmetry is treated as pseudocubic, and scattering was measured in the (*hhl*) plane.

Powder neutron diffraction was performed at the pulsed neutron diffractometers, NPDF of the Los Alamos Neutron Science Center and SEPD of the Intense Pulsed Neutron Source in Argonne National Laboratory. The powder samples were sealed with helium in vanadium cans and a hot-stage displex was used. The data were collected at four sets of detector banks. Rietveld refinement of the crystal structure was carried out using the GSAS computer programs[57] and the EXPGUI graphical interface.[58] The lattice parameters, phase fractions (when two phases were present), atomic positions, isotropic thermal parameters, background coefficients, and nonzero peak profile coefficients were refined. For PDF analysis, detailed background measurements were taken with the empty can, the displex, and a vanadium standard. From the Faber-Ziman structure function, $S(Q)$, the PDF, $\rho(r)$, was determined by Fourier transforming $S(Q)$ into real space:

$$\rho(r) = \rho_0 + \frac{1}{2\pi^2 r}\int_{Q_{min}}^{Q_{max}} Q[S(Q) - 1]\sin(Qr)dQ, \qquad (1)$$

where ρ_0 is the number density and Q_{max} is the maximum Q cutoff in the integral, 40 Å^{-1}. A damping function was used to ensure that the integrand smoothly approached 0 at Q_{max}. The steps in data analysis used to calculate $\rho(r)$ were carried out using the PDFGETN software.[59]

III. RESULTS AND DISCUSSION

A. Bulk properties

The field dependence of the magnetization measured from a powder and the resistivity measured from a sintered pressed pellet of $La_{0.8}Ca_{0.2}CoO_3$ are shown in Fig. 1. These results are in agreement with those reported earlier.[41] In Fig. 1(a), it can be seen that the magnetization increases below ~150 K, indicating a ferromagnetic transition.[60] It is evident that the magnetic transition temperature increases with an applied magnetic field. The saturation moment at 9 T is

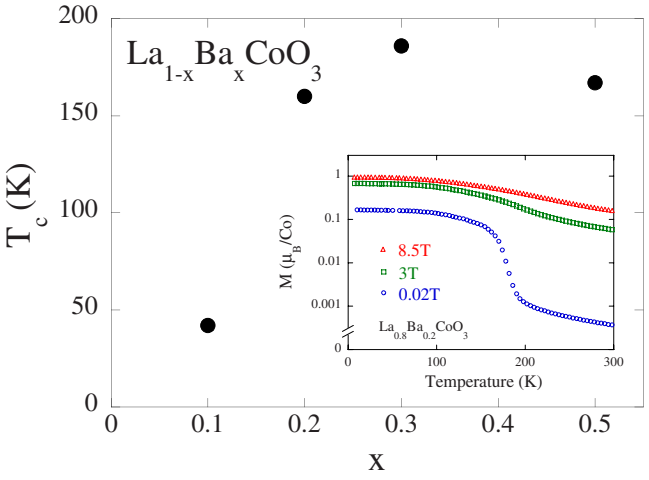

FIG. 2. (Color online) The transition temperature of LBCO as a function of x. The values of T_c were determined from the magnetization measurements. Above $x=0.2$, changing the doping concentration has little effect on T_c. Representative magnetization data ($x=0.2$) is shown in the inset under different applied fields.

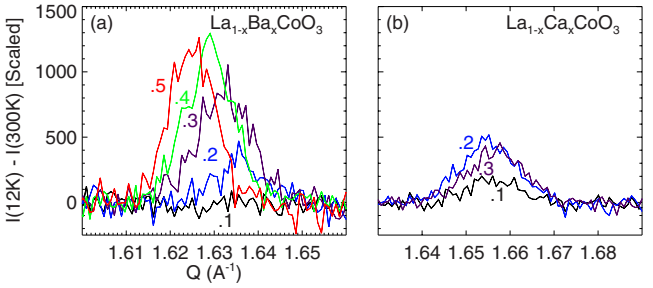

FIG. 3. (Color online) The scaled $(001)_c$ magnetic reflections as a function of doping for (a) LBCO and (b) LCCO. In LCCO, the Bragg peak first appears at $x=0.1$ and then saturates around $x=0.2$. On the other hand, in LBCO, the Bragg peak first appears at $x=0.2$ and continues to increase in intensity until $x=0.4$.

$\sim 1.09\mu_B$, a value which is too large to be from Co^{4+} alone, but is significantly smaller than that expected if all Co^{3+} ions were IS or HS, suggesting that there is a mixture of Co^{3+} ions in LS and IS and/or HS configurations. As the sample is cooled from room temperature, a broad hump is seen in the resistivity around T_c [Fig. 1(b)] corresponding to the transition to the magnetic state. As the temperature is lowered further, the resistivity undergoes an upturn and significantly increases as lower temperatures are approached. The temperature at which the upturn in resistivity occurs depends on the applied magnetic field; the upturn shifts to higher temperatures with increasing field.

The transition temperature as a function of x for LBCO powders is shown in Fig. 2. The transition temperature exhibits only a weak dependence on x above $x=0.2$. The magnetization as a function of field for the $x=0.2$ composition is shown in the inset of the figure. As can be seen in the inset, an applied field increases the transition temperature similar to the case of LCCO. The saturation moment in 8.5 T for $x=0.2$ is $\sim 0.95\mu_B$, which is reduced from the saturation moment of LCCO in 9.0 T field for the same concentration. However, this saturation moment increases upon doping to a value of $\sim 1.98\mu_B$ for $x=0.5$.

B. Magnetic diffraction

In the neutron scattering experiment, a magnetic contribution to the intensity will appear due to the interaction of the magnetic moment of the neutron with the magnetic moment of a crystal. In a magnetically ordered system, magnetic Bragg reflections will be observed in the diffraction pattern at temperatures below the transition. These are most easily seen by subtracting the base temperature patterns from the room temperature patterns. A particularly convenient reflection to study in this case is the $(001)_c$ reflection because the corresponding nuclear structure factor is so weak that no nuclear reflection is observed from the powder. Therefore, when the room temperature data are subtracted from the low-temperature data, only the magnetic reflection remains (we do not have to worry about the Debye-Waller factor, a change in the position of the reflection due to thermal expansion, or an orthorhombic to rhombohedral phase transition). The strength of the $(001)_c$ reflection should reflect the degree of ferromagnetic ordering. In order to accurately compare the relative strengths of this magnetic reflection from different samples, the magnetic reflection must be scaled by the strength of the nuclear scattering from the sample. The scattering from a nuclear reflection can be written as

$$I(Q) = \frac{I_N n_Q}{nV}|F_N(Q)|^2, \tag{2}$$

where I_N is a scaling strength factor, n_Q is the multiplicity of the Bragg reflection, n is the number of atoms in the unit cell, V is the volume of the unit cell, and $F_N(Q)$ is the nuclear structure factor for the Bragg reflection. I_N can be determined from a Bragg reflection and then used as a scaling factor. The $(220)_R$ peak at 12 K ($Q \sim 3.25$ Å^{-1}) was used to calculate I_N because it changes very little with the rhombohedral distortion. This peak splits into the $(202)_O$ and $(040)_O$ peaks in the *Pnma* phase, but the split cannot be observed within the resolution of the diffraction experiment.

The scaled $(001)_c$ magnetic reflections are shown as a function of doping in Fig. 3 for (a) LBCO and (b) LCCO. In LCCO, a weak Bragg peak appears in the sample with $x=0.1$. The Bragg peak increases in intensity up to $x=0.2$, at which point it appears to saturate because the intensity does not increase further with $x=0.3$. On the other hand, in LBCO, no magnetic Bragg peak is present in the $x=0.1$ sample, but in $x=0.2$, a weaker peak than in the LCCO reflection with the same concentration is observed. This is consistent with the smaller saturation moment of LCCO reported in Sec. III A. As the hole concentration is increased further, the Bragg peak continues to increase until $x=0.4$, becoming much stronger than the saturated value in LCCO. This indicates that a higher degree of ferromagnetic ordering can be achieved in the LBCO series.

The elastic neutron scattering data from a single crystal of $La_{0.95}Ca_{0.05}CoO_3$ are shown in Fig. 4. The scattering intensity observed at (001) is due to ferromagnetic correlations in

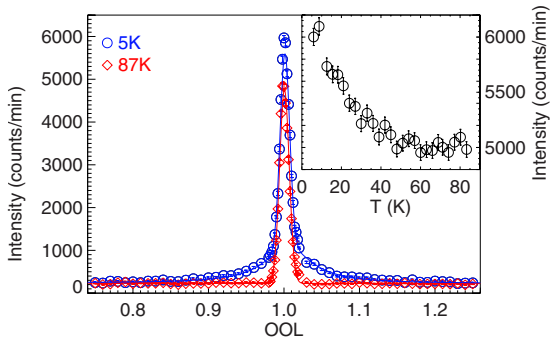

FIG. 4. (Color online) Elastic scattering along (00L) around (001) of $x=0.05$ of LCCO. At 5 K, a broad ferromagnetic intensity appears, indicating the presence of static, short-range ferromagnetic correlations. In the inset, the ferromagnetic order parameter is shown by measuring the temperature dependence of the (001) Bragg peak.

the crystal. At 5 K, broad ferromagnetic scattering is observed around the (001) reflection that is superimposed with nuclear scattering, while above the transition temperature, at 87 K, only nuclear scattering is present. The broadening occurs due to the finite length of the ferromagnetic correlations. Such scattering has also been observed in LSCO crystals in the spin-glass phase.[28] Since the magnetic scattering is much broader than the instrumental resolution, the correlation length can be estimated as the inverse of the half-width half maximum of a Lorentzian fit to the scattering. We estimate that at 5 K the correlation length is ~16 Å. This correlation length is significantly larger than that observed in LSCO for the same doping concentration, and corresponds to the correlation length found in $x=0.1-0.15$ of the LSCO system. Our observation of a finite correlation length indicates that the magnetic state of $La_{0.95}Ca_{0.05}CoO_3$ is a spin-glass state, rather than a ferromagnet, and conflicts a previous report of Ref. 41. The order parameter of the ferromagnetic scattering as measured at (001) is shown in the inset of the figure.

C. Crystal structure

The neutron powder diffraction patterns of LCCO were refined using two crystal phases, *Pnma* and $R\bar{3}c$. In Table I, the refined phase fractions, lattice parameters, and atomic positions are listed for a number of temperatures and concentrations. Based on this refinement and from results reported by Burley *et al.*,[53] a structural phase diagram is constructed, which is shown in Fig. 5(a). At low temperatures, a phase transition occurs from $R\bar{3}c$ to *Pnma* as a function of doping, with a considerably large region in between where the $R\bar{3}c$ and *Pnma* phases coexist. For $x=0.1$, mixed $R\bar{3}c$ and *Pnma* phases are observed from ~100 K and below, though we estimate that the phase fraction of *Pnma* was less than 5% 10 K; at 300 K, only the $R\bar{3}c$ phase is present. For $x=0.15$,[53] a mixed phase is observed, but at $x \geqslant 0.2$, the low-temperature phase is entirely *Pnma*. Close to room temperature, mixed phases are observed for concentrations of $x \geqslant 0.2$; at higher temperatures, the crystal transforms entirely to the $R\bar{3}c$ phase. The corresponding crystal structures for $R\bar{3}c$ and *Pnma* are shown in Figs. 5(b) and 5(c). The unit cell volumes and Co-O-Co bond angles are plotted in Fig. 6 as a

TABLE I. The results of the Rietveld refinement for $La_{1-x}Ca_xCoO_3$. The listed parameters are defined as follows: f_R, phase fraction of $R\bar{3}c$; a_R and α_R, $R\bar{3}c$ lattice constants; f_O, phase fraction of *Pnma*; and a_o, b_o, and c_o, *Pnma* lattice constants. The (6*e*) O position for $R\bar{3}c$ is given by $(x_R^O, \frac{1}{2}\text{-}x_R^O, \frac{3}{4})$; the (4*c*) La/Ca position for *Pnma* is given by $(x_O^{La}, \frac{1}{4}, z_O^{La})$; the (4*c*) O position for *Pnma* is given by $(x_O^{O1}, \frac{1}{4}, z_O^{O1})$; and the (8*d*) O position for *Pnma* is given by $(x_O^{O2}, y_O^{O2}, z_O^{O2})$.

	$x=0.1$		$x=0.2$			$x=0.3$		
	10 K	300 K	10 K	300 K	550 K	10 K	300 K	550 K
f_R	>95%	100%	0%	58%	100%	0%	46%	100%
a_R(Å)	5.347	5.373		5.372	5.394		5.371	5.390
α_R	60.941°	60.765°		60.724°	60.601°		60.613°	60.475°
f_O	<5%	0%	100%	42%	0%	100%	54%	0%
a_O(Å)			5.366	5.380		5.360	5.374	
b_O(Å)			7.605	7.621		7.599	7.614	
c_O(Å)			5.415	5.430		5.404	5.413	
x_R^O	0.198	0.200		0.199	0.202		0.198	0.203
x_O^{La}			0.017	0.014		0.014	0.011	
z_O^{La}			−0.003	−0.001		−0.001	0.000	
x_O^{O1}			0.496	0.497		0.497	0.498	
z_O^{O1}			0.059	0.057		0.060	0.053	
x_O^{O2}			0.272	0.269		0.271	0.269	
y_O^{O2}			0.031	0.030		0.030	0.030	
z_O^{O2}			0.729	0.732		0.730	0.732	

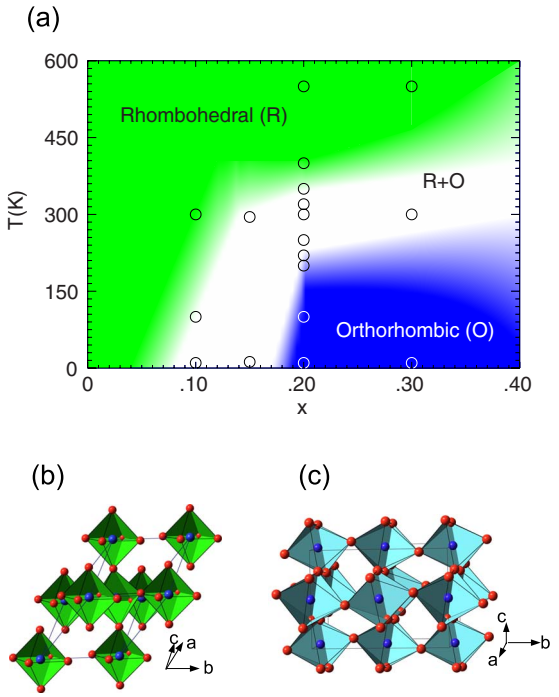

FIG. 5. (Color online) (a) The LCCO structural phase diagram. Circles indicate where data points were taken. The data points for $x=0.15$ are taken from Ref. 53. The fading between colors is intended to represent the uncertainty in the phase diagram. (b) The crystal model for the $R\bar{3}c$ phase. (c) The crystal model corresponding to the *Pnma* phase. Only the Co-O octahedra are shown.

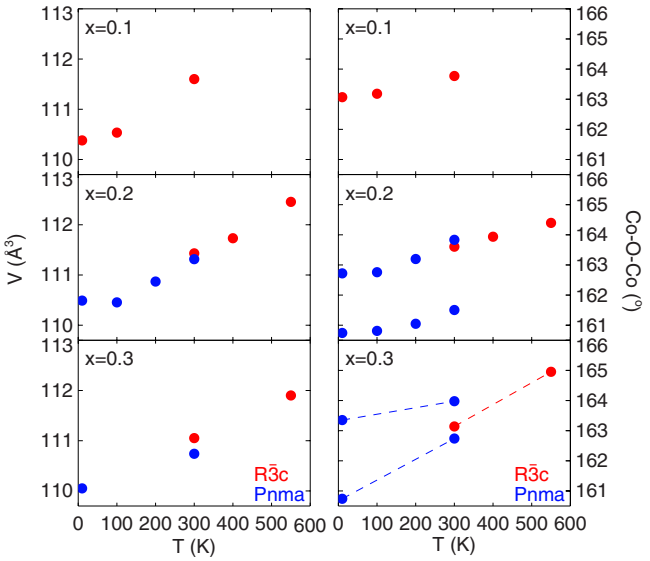

FIG. 6. (Color online) Results of the Rietveld refinement of LCCO as a function of temperature and concentration: (a) the unit cell volume and (b) the Co-O-Co bond angles. Values derived from the *Pnma* phase are shown in blue, while values from the $R\bar{3}c$ phase are shown in red. The unit cell volume for the *Pnma* phase has been divided by 2 due to the fact that it has twice as much volume as the $R\bar{3}c$ unit cell.

function of temperature for three concentrations. For all the temperatures and compositions measured, the Co-O-Co angle lies between 160° and 165°. For $x=0.1$, where the structure is at least 95% rhombohedral with $R\bar{3}c$ symmetry, the Co-O-Co angles undergo a relatively minor increase with temperature. However, for the $x=0.2$ and 0.3 samples, there are two different Co-O-Co bond angles in the *Pnma* phase. The concentrations that undergo a structural phase transition exhibit a more pronounced temperature dependence of the bond angles.

The crystal structure of LBCO was refined to be of the $R\bar{3}c$ phase for all temperatures and concentrations, and the results are listed in Table II. In the rhombohedral setting, the degree of trigonal distortion that results from the tilting of the oxygen octahedra about the cubic (111) axis can be well described by the rhombohedral angle α. This is plotted in Fig. 7(a) as a function of temperature for five different compositions. The refinement indicates that the degree of trigonal distortion is reduced both with increasing x and temperature. The samples with $x=0.4$ and 0.5 become almost cubic by 500 K. The lattice volume increases significantly with doping due to the large size of the Ba^{2+} ions (not shown). As the trigonal distortion is reduced, the Co-O-Co angle approaches 180° with increasing x. Earlier reports suggested that the crystal symmetry of $La_{0.5}Ba_{0.5}CoO_3$ is monoclinic below T_c due to cooperative JT ordering,[54] which is in contradiction to our observation of an $R\bar{3}c$ phase using the NPDF instrument. It is possible that the crystal structure is sensitive to oxygen stoichiometry so that differences in the sample synthesis procedure could affect the crystal symmetry. Recently, it was shown that the different magnetic, electronic, and structural phases could be tuned by the oxygen stoichiometry in $La_{1/3}Sr_{2/3}CoO_{3-\delta}$,[61] while similar effects were previously shown for the manganites.[62]

The size effect of the A-site cation plays an important role in the magnetic and transport properties. In LCCO, where the nominal size of Ca^{2+} ions is smaller than La^{3+}, the substitution induces a reduction in the crystal symmetry. On the other hand, in LBCO, the Ba^{2+} ion is significantly bigger than La^{3+} and the trigonal distortion is reduced with doping. This can be understood by the tolerance factor:[63]

$$t = \frac{\mathrm{A-O}}{\sqrt{2}(\mathrm{B-O})} \tag{3}$$

where A-O corresponds to the bond length between the cation at the A-site and oxygen, and B-O corresponds to the bond length between the cation at the B site and oxygen in the ABO_3 perovskite structure. One often observes that in perovskites, the symmetry of the structure is lowered to rhombohedral or orthorhombic from the cubic aristotype when $t<1$, and this is the case for LCCO. However, the addition of large Ba^{2+} ions in LBCO increases the A-O bond length, allowing t to approach 1 and, thus, the trigonal distortion to be reduced. It has been shown that the A-O bond expands more than the B-O bonds in many transition metal perovskites, which also allows t to approach 1.[63] This explains the reduction of the trigonal distortion observed in LBCO and LCCO (see the refined values of α in Tables I and II) as the temperature is increased. The change in the unit

TABLE II. The results from the Rietveld refinement for $La_{1-x}Ba_xCoO_3$. The listed parameters refer to the $R\bar{3}c$ phase. The (6*e*) O position is given by $\left(x_R^O, \frac{1}{2}-x_R^O, \frac{3}{4}\right)$.

x	T (K)	a (Å)	α	V (Å^3)	x_R^O
0.1	12	5.390	60.721	112.6	0.205
	300	5.413	60.575	113.6	0.207
	500	5.434	60.490	114.7	0.209
0.2	12	5.424	60.439	114.0	0.213
	300	5.440	60.351	114.8	0.216
	500	5.458	60.274	115.7	0.219
0.3	12	5.447	60.182	114.8	0.225
	300	5.463	60.132	115.6	0.228
	500	5.477	60.088	116.4	0.233
0.4	12	5.461	60.182	115.3	0.236
	300	5.478	60.061	116.4	0.242
	500	5.491	60.080	117.2	0.246
0.5	12	5.476	60.077	116.3	0.246
	300	5.494	60.072	117.4	0.247
	500	5.508	60.068	118.4	0.248

cell volume is minimal with doping in LCCO, but a large increase is observed in LBCO due to the large difference in the A-site ion size between La^{3+} and Ba^{2+}. The straightening of bond angles in LBCO may result in the higher degree of ferromagnetic ordering of LBCO with respect to LCCO, as discussed in Sec. III B.

D. Local atomic structure

The PDF, $\rho(r)$, contains information on the interatomic correlations in crystals represented in real space. The experimentally determined PDFs are compared to the model PDFs calculated from[64]

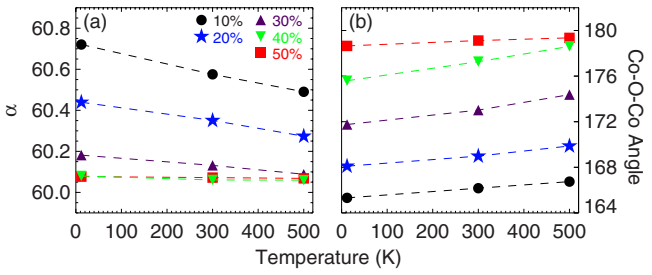

FIG. 7. (Color online) Results of Rietveld refinement of LBCO as a function of temperature and concentration. The $R\bar{3}c$ lattice parameter, α, is shown in (a). The deviation of α from the cubic value of 60° provides an indication of the degree of trigonal distortion. It is clear that either increasing the temperature or increasing the doping reduces the degree of trigonal distortion. In (b), the Co-O-Co bond angles are shown. These bonds significantly straighten with doping.

$$\rho(r) = \frac{1}{4\pi r^2} \sum_{ij} \frac{b_i b_j}{\langle b \rangle^2} \delta(r - r_{ij}) \tag{4}$$

that uses unit cell dimensions and atomic coordinates determined from the Rietveld analysis as input to the model. The sum is taken over all pairs of atoms i and j, b_j is the neutron scattering length for the jth atom, and $\langle b \rangle$ is the average scattering length. The finite instrumental resolution and atomic vibrations lead to broadening of the delta functions. No assumption of periodicity need be made to obtain $\rho(r)$, so this function describes the local atomic structure rather than the average, long-range crystal structure. In Fig. 8(a), the experimentally determined $\rho(r)$ is plotted for $La_{0.9}Ba_{0.1}CoO_3$ along with a model based on the crystal structure determined by Rietveld refinement assuming a Gaussian broadening of the delta functions. The model can be decomposed into partial PDFs corresponding to bonds between different types of atoms, as shown in Fig. 8(b), where the total PDF is equal to the sum of all the partial PDFs. While there is some discrepancy between the experimental PDF and the model in the widths of the peaks (this is because all experimental peaks do not have the same width), all peaks in the experimental PDF are reproduced by the model PDF, and there is good agreement between the local atomic structure and the long-ranged crystal structure.

From Fig. 8(b), it can be seen that the first peak in the PDF is well isolated from all other peaks and corresponds to the nearest neighbor (octahedral) Co-O bonds. The region of the PDF corresponding to the octahedral Co-O bonds is plotted at 12, 300, and 500 K for LBCO in Fig. 9. At 12 K, the Co-O peaks appear to be almost symmetric, signifying that there is only one type of Co-O bond length at the concentra-

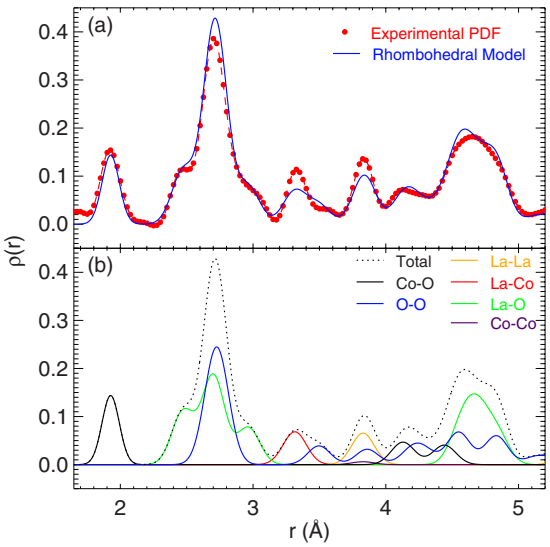

FIG. 8. (Color online) (a) Experimental and model PDFs for $La_{0.9}Ba_{0.1}CoO_3$ at 12 K. (b) The model partial PDFs indicate the pairs of atoms that contribute to the various peaks in the PDF. The sum of all the partial PDFs gives rise to the total model PDF and is compared to the experimental data of (a). Note that the first peak in the PDF has no other contribution than from the Co-O bonds.

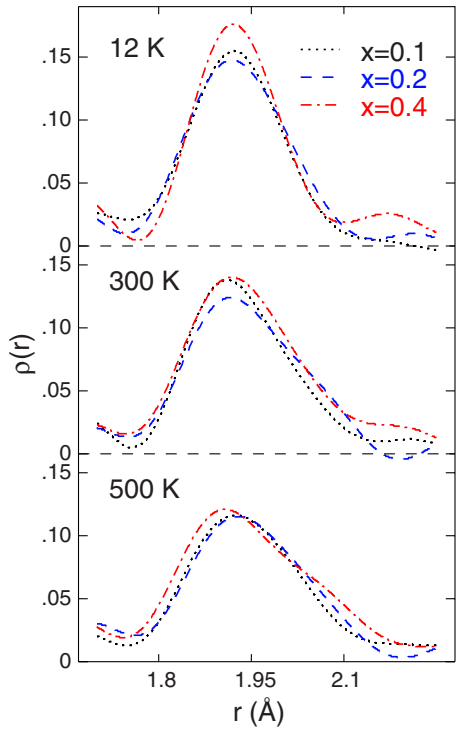

FIG. 9. (Color online) The first PDF peak corresponding to the Co-O octahedral bonds is shown at $T=12$, 300, and 500 K for the LBCO system at three different concentrations. The nearly symmetric peak at 12 K broadens asymmetrically at 300 and 500 K due to the formation of a shoulder on the right side. This is observed for all x.

tions shown. The Co-O peaks are expected to broaden symmetrically if the broadening is simply due to increased thermal vibrations with increasing temperature. However, this is not the case as a clear asymmetry is present at the 300 and 500 K data shown; the asymmetry comes from the formation of a shoulder on the right side of the Co-O peak due to the formation of long Co-O bonds. The effect is apparent at $x=0.1$ at 300 K, but is even more pronounced at $x=0.2$ and $x=0.4$. The development of a shoulder in the PDF indicates that the Co-O bonds are split into long and short bonds when the temperature is increased.

The split of the Co-O bond is a consequence of static JT distortions invoked in order to break the e_g orbital degeneracy that, in turn, stabilizes the IS state. With doping, some of the Co^{3+} ions ($t_{2g}^6 e_g^0$) in the ground state nominally transform to Co^{4+} ($t_{2g}^5 e_g^0$) proportionally with x. The rest of the Co^{3+} ions can either stay in the LS state or activate to the IS or HS states. The static JT distortion resulting from the single occupancy of the e_g orbital can be either from $Co^{3+}(t_{2g}^5 e_g^1)$-O or $Co^{4+}(t_{2g}^4 e_g^1)$-O complexes or both. In order to estimate the number of sites that are JT active, the octahedral Co-O peaks in the PDFs were fitted by Gaussian functions as shown in Fig. 10. At 12 K, the PDFs for $x=0.1$, 0.2, 0.3, and 0.4 in LBCO were fitted by a single Gaussian function due to their relatively symmetric peak shapes. At 300 and 500 K, the asymmetry becomes clear and two Gaussian functions were used to fit the PDFs, except for the $x=0.3$ PDFs which did not show any significant asymmetry. The $x=0.3$ is a unique case, and similar observations were made for this composition in the LSCO system in Ref. 14. For $x=0.5$, the peak asymmetry extends all the way down to 12 K, so two Gaussians were used to fit the 12 and 300 K data. However, at 500 K, significant intensity is observed on the left side of the main Co-O PDF peak that prevented a reasonable fit by either two Gaussian functions; therefore, it was fitted by three Gaussian functions. This shows that there are three Co-O bonds for the 50% LBCO sample at 500 K. Since there are a number of ways to fit multiple Gaussians to the data with a similar quality of fit, constraints of the fitting parameters were applied. When two or three Gaussian functions were used to fit the PDFs, the Gaussian used to fit the short bonds was constrained to have the same σ as the one used to fit the short Co-O bonds in $x=0.1$ at 12 K. This composition was chosen because the Co-O peak was symmetric. The constraint was relaxed for one case, the $x=0.2$ at 300 K that required a σ that was smaller than the constrained value. The fitted peak positions are shown in Fig. 11 along with the Co-O bond lengths obtained from the Rietveld refinement. At 12 K, there is very good agreement between the average bond length and those obtained from local atomic structure of $x=0.1$, 0.2, 0.3, and 0.4. For $x=0.5$, however, two Co-O bonds are present even at 12 K. At higher temperatures, only one average bond length is obtained from the Rietveld refinement, while two bond lengths are obtained from the PDF analysis up to $x=0.4$. The average bond length is close to the short Co-O bonds. In the case of $x=0.5$, three local bond lengths are obtained from the PDF analysis at 500 K, while the average bond length matches only the middle local bond length obtained from the three Gaussian fits of the PDF.

Since the octahedral Co-O peaks are well separated from any other peak in the PDF, the number of bonds that contribute to the Co-O peak can be calculated from

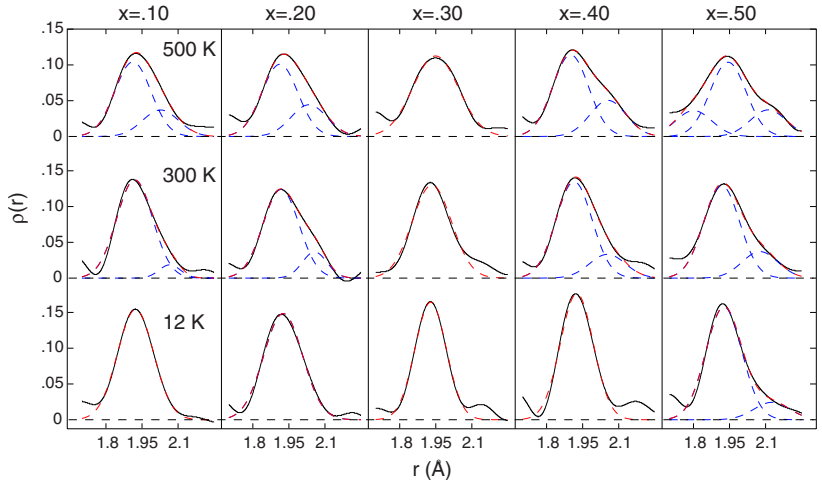

FIG. 10. (Color online) Gaussian fits of the Co-O experimental peak for LBCO at several different concentrations and as a function of temperature. The experimental data are shown in solid line and the Gaussian fits are shown in dotted lines.

$$N_i = \frac{\langle b \rangle^2}{2c_{\mathrm{Co}} b_{\mathrm{O}} b_{\mathrm{Co}}} \int 4\pi r^2 \rho(r) dr, \tag{5}$$

where the index i denotes either the short bond or long bond, and c_{Co} is the Co concentration in the unit cell. Because this is a perovskite structure, the sum of short and long bonds should be 6. Assuming that a JT active Co ion has four short bonds and two long bonds, the fraction of Co ions which are JT active is given by

$$f_{JT} = N_{long}/2. \tag{6}$$

The fraction of JT active Co ions is shown in Fig. 12 as a function of temperature and concentration for LBCO. At the lowest temperature, no JT sites are active up to $x=0.4$. This serves as a strong indication that the Co^{4+} ion introduced in the lattice with the substitution of trivalent La^{3+} is not JT active; otherwise, one would expect even at the lowest measured temperature a one-to-one correspondence of JT active ions with doping, x. For $x=0.5$ however, there are JT distortions even at 12 K, where we estimate that nearly 50% of the ions are JT active. With increasing temperature, the percentage of JT sites increases rapidly with x. Increasing the temperature even further almost saturates the lattice with JT sites as almost all sites are JT distorted for almost all x. This result is quite surprising as it would suggest that both Co^{3+} and Co^{4+} ions are JT distorted by 500 K. Looking at compositions individually, for $x=0.1$, only a small fraction (approximately 25%) of the Co ions are JT active at 300 K. However, at 500 K, the fraction increases significantly and nearly all of the Co ions are JT active. As x is increased to 0.2, the fraction of JT active ions increases to approximately 55% at 300 K. Neglecting the $x=0.3$ data, the fraction slowly increases with further increase in x at 300 K and reaches a value of 75% at $x=0.5$. By 500 K, almost all sites are distorted. The $x=0.5$ sample deserves special attention and will be discussed in a forthcoming paper.

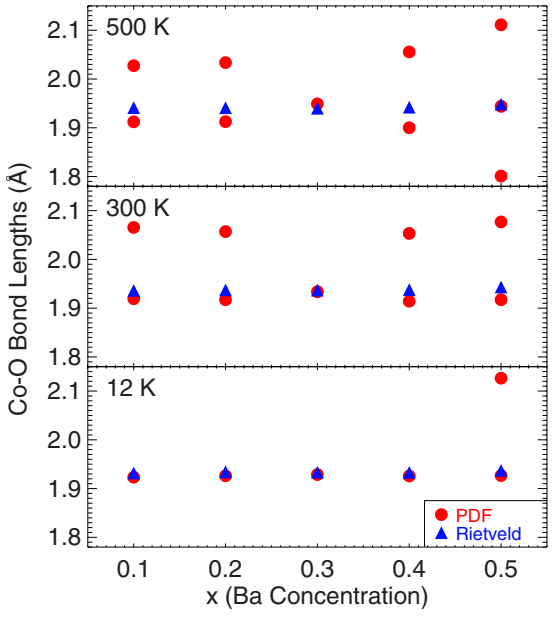

FIG. 11. (Color online) The Co-O bond length as a function of x of the LBCO system. The bondlengths derived from fits of the PDFs are shown in solid circles, while the bond lengths from Rietveld refinement are shown in solid triangles.

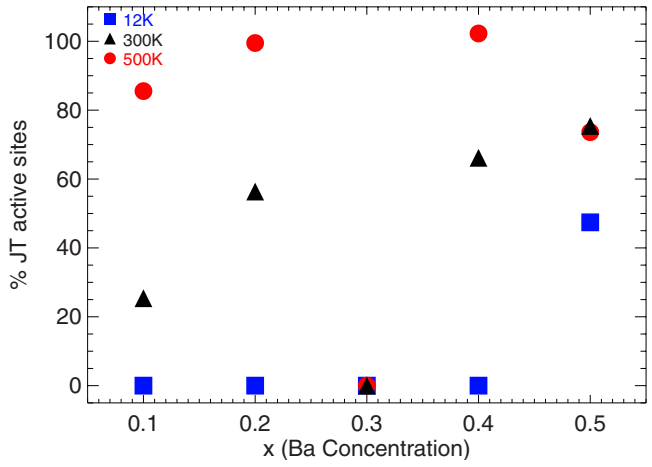

FIG. 12. (Color online) The percent of JT active sites in the LBCO system obtained from the integrated intensity of the area under the Co-O peaks at 12, 300, and 500 K.

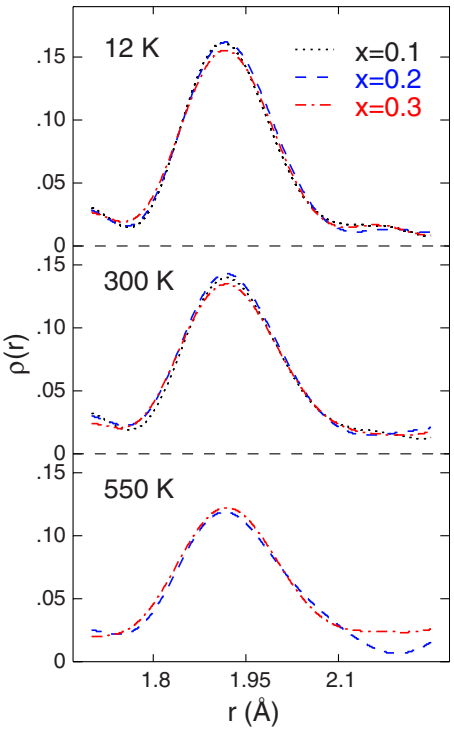

FIG. 13. (Color online) The first PDF peak corresponding to the Co-O octahedral bonds is shown for LCCO at 10, 300, and 550 K. The peaks are somewhat asymmetric, but are not as asymmetric and do not show a clear split as in the LBCO system.

The temperature and compositional dependence of the local atomic structure of LCCO is shown in the region in space that includes the octahedral Co-O peaks (Fig. 13). At 12 K, there is a single Co-O bond length at all x. Note that the $x=0.1$ composition is predominantly rhombohedral at this temperature, whereas the $x=0.2$ and 0.3 compositions are entirely orthorhombic. This shows that the rhombohedral to orthorhombic phase transition has little effect on the Co-O bonds. At 300 K, while the crystal structure changes with x, the data can be fitted well with a single Co-O peak. At 550 K, it is clear that a distinct shoulder appears at $x=0.2$, signifying the development of long Co-O bonds as in LBCO. The fits for the LCCO PDFs are shown in Fig. 14. The fraction of JT active ions in $x=0.2$ LCCO at 550 K is estimated to be nearly 100%. At the same time, the Co-O peak in the $x=0.3$ sample appears symmetric at all temperatures as in LBCO and LSCO.[14]

Our estimate of the fraction of JT active ions based on the bond splitting clearly shows that it increases rapidly with temperature. This is consistent with the thermal population of the IS state. This indicates that if all sites are JT active, then both Co^{3+} and Co^{4+} ions must be in the IS state. The question that arises from this is what happens at low temperatures. No sample other than the $x=0.5$ sample in the LBCO system shows a clear evidence for JT active ions at 12 K. This may be related to dynamics where the e_g orbitals and the lattice are coupled dynamically by phonons that result in events outside the integration window of the diffraction experiment. As a result, the peaks appear symmetric as in the $x=0.3$ case for all temperatures because of dynamics.

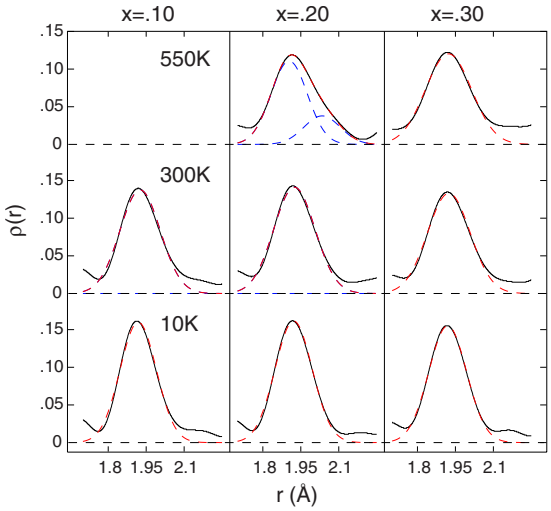

FIG. 14. (Color online) Gaussian fits of the Co-O experimental peak for LCCO at several different concentrations as a function of temperature. The octahedral Co-O bonds are reasonably well fitted with one Gaussian except for the $x=0.20$ at 550 K, where a clear long Co-O bond length is observed.

When dynamic events occur within an energy window that is close to the energy integration limits set by the kinematics of the experiment, the PDF fluctuates erratically. Typically, the PDF can be determined from data collected at individual detector banks, without merging all groups together, and shows very little change from one detector group to another. However, in the case where dynamical fluctuations are present in the system, the PDF varies significantly with detector group because the integration window changes with angle. This serves as an indication that dynamic processes occur. The dependence of PDF on dynamics has been previously discussed in Refs. 14 and 45. At the same time, the low-temperature phase is associated with metallic transport, where charges are not likely to be localized on one Co site for long to create localized IS states.

Our room temperature data for LBCO suggest that increasing the doping levels results in a larger population of stabilized IS ions since the trend is for the estimated fraction of JT ions to increase with doping. However, for the same levels of doping, less asymmetry is observed in the LCCO series, which eliminates the variables of hole concentration and temperature and shows explicitly that the stabilization of IS is dependent on structural changes that occur due to differently sized dopants. Namely, the stabilization of IS appears enhanced by a straightening of the Co-O-Co angles and the expansion of the lattice.

There are two possible ways that may contribute to the stability of the IS state. One is through the formation of seven-site magnetopolarons as discussed in Refs. 45 and 46. If the Co^{4+}-O^{2-} octahedra contract because of the somewhat smaller size of Co^{4+} ion, then the IS state can be stabilized on the six nearest neighboring Co^{3+} ions.[45] How far the magnetopolarons can propagate through the lattice may depend on a second mechanism which depends on the crystal structure. One could wonder how do Co^{3+} ions that are far away from Co^{4+} sites, such as in hole-poor regions, become af-

fected thermally. Take the undoped cobaltite, $LaCoO_3$, and then start reducing the trigonal distortion, straightening the Co-O-Co bonds, and expanding the lattice (without holes): these effects will affect the competing energy mechanisms that determine whether IS and/or HS or LS is the ground state. In the case of LCCO, the magnetopolarons appear to be more localized, and this may be associated with the small size of Ca^{2+} ion. In the case of LBCO, the magnetopolarons become extended, aided by key structural changes described above. It is also the case that the Co-O split in LCCO is smaller than in LBCO.

IV. CONCLUSIONS

The results discussed in this paper reveal that there are a number of important differences in the magnetic, transport, and structural properties of cobaltites with differently sized dopants. The most fundamental difference between LCCO and LBCO is that, starting from a rhombohedral parent, the crystal structure of LCCO undergoes a reduction in symmetry to an orthorhombic phase at low temperatures with doping, whereas the crystal structure of LBCO steadily approaches the cubic aristotype with doping. As a result, the Co-O-Co bonds remain significantly bent in LCCO but become straightened in LBCO, and the lattice volume significantly expands in LBCO, whereas it does not in LCCO. These points form a basis which can be used to explain the differences in electronic and bulk properties between the two series.

The crystallographic effects have an impact on the development of ferromagnetism and metallicity. In LCCO, ordered ferromagnetism appears for as little doping as $x=0.1$, evidenced by the appearance of a (001) ferromagnetic Bragg peak in the neutron diffraction pattern. However, the (001) peak saturates to a weak value around $x=0.2$, near the point where the crystal structure becomes fully orthorhombic at low temperature. Thus, it is likely that the orthorhombic phase transition inhibits further development of ferromagnetism with doping in LCCO. The bent Co-O-Co bonds restrain the double-exchange mechanism and charge hopping, a notion which is further strengthened by the transport measurements of LCCO, where an upturn in the resistivity, characteristic of insulating behavior, is observed below 100 K in $La_{0.8}Ca_{0.2}CoO_3$. The field effect on the upturn temperature causes positive magnetoresistance below 100 K. Since this positive magnetoresistance had not been observed in previous reports of LBCO or LSCO, this suggests that this effect is directly related to the orthorhombic phase transition in LCCO. On the other hand, ordered ferromagnetism is slower to appear in LBCO, where a weak Bragg peak is first observed around $x=0.2$; nevertheless, this peak continues to increase with doping and saturates with a much larger magnitude around $x=0.4$. Thus, the continued straightening of Co-O-Co bonds in LBCO enhances the double-exchange mechanism, which promotes ferromagnetic ordering. To conclude, our analysis of the local structures uncovered a thermally induced asymmetry in the Co-O bonds in both series, which we argue results from the presence of JT active IS ions. We suggest that IS ions are stabilized by (1) the formation of magnetopolarons in hole-rich regions and (2) by long-range crystallographic changes in hole-poor regions.

ACKNOWLEDGMENTS

The authors would like to acknowledge T. Proffen and P. Encinias for their assistance with the NPDF diffractometer at the Los Alamos National Laboratory, J. Fieramosca and R. Kiyanagi of Argonne National Laboratory for help with the SEPD diffractometer, and J.-H. Chung for help with SPINS at the NIST Center for Neutron Research. The work at the University of Virginia is supported by the U.S. Department of Energy under Contract No. DE-FG02-01ER45927. Work performed at Los Alamos National Laboratory was performed under the auspices of the U.S. Department of Energy and at the NIST Center for Neutron Research under National Science Foundation Contract No. DMR-0454672.

[1] E. Dagotto, Science **309**, 257 (2005).
[2] J. Tranquada, B. J. Sternlieb, J. Axe, Y. Nakamura, and S. Uchida, Nature (London) **375**, 561 (1995).
[3] J. B. Goodenough, J. Phys. Chem. Solids **6**, 287 (1958).
[4] G. Blasse, J. Appl. Phys. **36**, 879 (1965).
[5] P. M. Raccah and J. B. Goodenough, Phys. Rev. **155**, 932 (1967).
[6] N. Menyuk, K. Dwight, and P. M. Raccah, J. Phys. Chem. Solids **28**, 549 (1967).
[7] V. G. Bhide, D. S. Rajoria, G. R. Rao, and C. N. R. Rao, Phys. Rev. B **6**, 1021 (1972).
[8] K. Asai, P. Gehring, H. Chou, and G. Shirane, Phys. Rev. B **40**, 10982 (1989).
[9] M. A. Korotin, S. Y. Ezhov, I. V. Solovyev, V. I. Anisimov, D. I. Khomskii, and G. A. Sawatzky, Phys. Rev. B **54**, 5309 (1996).
[10] T. Saitoh, T. Mizokawa, A. Fujimori, M. Abbate, Y. Takeda, and M. Takano, Phys. Rev. B **55**, 4257 (1997).
[11] S. Stolen, F. Gronvold, H. Brinks, T. Atake, and H. Mori, Phys. Rev. B **55**, 14103 (1997).
[12] K. Asai, A. Yoneda, O. Yokokura, J. M. Tranquada, G. Shirane, and K. Kohn, J. Phys. Soc. Jpn. **67**, 290 (1998).
[13] M. Zhuang, W. Zhang, and N. Ming, Phys. Rev. B **57**, 10705 (1998).
[14] D. Louca, J. L. Sarrao, J. D. Thompson, H. Roder, and G. H. Kwei, Phys. Rev. B **60**, 10378 (1999).
[15] Y. Kobayashi, N. Fujiwara, S. Murata, K. Asai, and H. Yasuoka, Physica B **281**, 512 (2000).
[16] Y. Kobayashi, N. Fujiwara, S. Murata, K. Asai, and H. Yasuoka, Phys. Rev. B **62**, 410 (2000).
[17] P. Ravindran, H. Fjellvag, A. Kjekshus, P. Blaha, K. Schwarz, and J. Luitz, J. Appl. Phys. **91**, 291 (2002).
[18] S. Noguchi, S. Kawamata, K. Okuda, H. Nojiri, and M. Motokawa, Phys. Rev. B **66**, 094404 (2002).
[19] C. Zobel, M. Kriener, D. Bruns, J. Baier, M. Gruninger, T. Lorenz, P. Reutler, and A. Revcolevschi Phys. Rev. B **66**, 020402

(2002).
[20] G. Maris, Y. Ren, V. Volotchaev, C. Zobel, T. Lorenz, and T. T. M. Palstra, Phys. Rev. B **67**, 224423 (2003).
[21] T. Kyomen, Y. Asaka, and M. Itoh, Phys. Rev. B **67**, 144424 (2003).
[22] I. A. Nekrasov, S. V. Streltsov, M. A. Korotin, and V. I. Anisimov, Phys. Rev. B **68**, 235113 (2003).
[23] A. Ishikawa, J. Nohara, and S. Sugai, Phys. Rev. Lett. **93**, 136401 (2004).
[24] M. Magnuson, S. M. Butorin, C. Sathe, J. Nordgren, and P. Ravindran, Europhys. Lett. **68**, 289 (2004).
[25] V. P. Plakhty, P. J. Brown, B. Grenier, S. V. Shiyaev, S. N. Barilo, S. V. Gavrilov, and E. Ressouhe, J. Phys.: Condens. Matter **18**, 3517 (2006).
[26] T. Kyomen, Y. Asaka, and M. Itoh, Phys. Rev. B **71**, 024418 (2005).
[27] K. Kniaek, P. Novak, and Z. Jirak, Phys. Rev. B **71**, 054420 (2005).
[28] D. Phelan *et al.*, Phys. Rev. Lett. **96**, 027201 (2006).
[29] V. Gnezdilov, V. Fomin, A. V. Yeremenko, K. Y. Choi, Y. Pashkevich, P. Lemmens, S. Shiryaev, G. Bychkov, and S. Barilo, Low Temp. Phys. **32**, 162 (2006).
[30] M. W. Haverkort *et al.*, Phys. Rev. Lett. **97**, 176405 (2006).
[31] A. Podlesnyak, S. Streule, J. Mesot, M. Medarde, E. Pomjakushina, K. Conder, A. Tanaka, M. W. Haverkort, and D. I. Khomskii, Phys. Rev. Lett. **97**, 247208 (2006).
[32] A. Podlesnyak, K. Conder, E. Pomjakushina, A. Mirmelstein, P. Allenspach, and D. I. Khomskii, J. Magn. Magn. Mater. **310**, 1552 (2007).
[33] G. H. Jonker and J. H. V. Santen, Physica (Amsterdam) **19**, 120 (1953).
[34] P. M. Raccah and J. B. Goodenough, J. Appl. Phys. **39**, 1209 (1968).
[35] V. G. Bhide, D. S. Rajoria, C. N. R. Rao, G. R. Rao, and V. G. Jadhao, Phys. Rev. B **12**, 2832 (1975).
[36] M. Itoh, I. Natori, S. Kubota, and K. Motoya, J. Phys. Soc. Jpn. **63**, 1486 (1994).
[37] M. A. Senaris-Rodriguez and J. B. Goodenough, J. Solid State Chem. **118**, 323 (1995).
[38] C. Zock, L. Haupt, K. Barner, B. M. Todris, K. Asadov, E. A. Zavadskii, and T. Gron, J. Magn. Magn. Mater. **150**, 253 (1995).
[39] K. Muta, Y. Kobayashi, and K. Asai, J. Phys. Soc. Jpn. **71**, 2784 (2002).
[40] J. Wu and C. Leighton, Phys. Rev. B **67**, 174408 (2003).
[41] M. Kriener, C. Zobel, A. Reichl, J. Baier, M. Cwik, K. Berggold, H. Kierspel, O. Zabara, A. Freimuth, and T. Lorenz, Phys. Rev. B **69**, 094417 (2004).
[42] P. Mandal, P. Choudhury, S. K. Biswas, and B. Ghosh, Phys. Rev. B **70**, 104407 (2004).
[43] C. Zener, Phys. Rev. **81**, 440 (1951).
[44] C. N. R. Rao, A. Arulraj, A. K. Cheetham, and B. Raveau, J. Phys.: Condens. Matter **12**, R83 (2000).
[45] D. Louca and J. L. Sarrao, Phys. Rev. Lett. **91**, 155501 (2003).
[46] D. Phelan, D. Louca, K. Kamazawa, S.-H. Lee, S. Rosenkranz, M. F. Hundley, J. F. Mitchell, Y. Motome, S. N. Ancona, and Y. Moritomo, Phys. Rev. Lett. **97**, 235501 (2006).
[47] R. D. Shannon, Acta Crystallogr., Sect. A: Cryst. Phys., Diffr., Theor. Gen. Crystallogr. **A32**, 751 (1976).
[48] Q. Huang, A. Santoro, J. W. Lynn, R. W. Erwin, J. A. Borchers, J. L. Peng, and R. L. Greene, Phys. Rev. B **55**, 14987 (1997).
[49] G. Thornton, B. C. Tofield, and A. W. Hewat, J. Solid State Chem. **61**, 301 (1986).
[50] P. G. Radaelli and S. W. Cheong, Phys. Rev. B **66**, 094408 (2002).
[51] V. G. Sathe, A. V. Pimpale, V. Siruguri, and S. K. Paranjpe, J. Phys.: Condens. Matter **8**, 3889 (1996).
[52] R. Caciuffo, D. Rinaldi, G. Barucca, J. Mira, J. Rivas, M. A. Senaris-Rodriguez, P. G. Radaelli, D. Fiorani, and J. B. Goodenough, Phys. Rev. B **59**, 1068 (1999).
[53] J. C. Burley, J. F. Mitchell, and S. Short, Phys. Rev. B **69**, 054401 (2004).
[54] F. Fauth, E. Suard, and V. Caignaert, Phys. Rev. B **65**, 060401(R) (2001).
[55] S. K. Pandy, S. Khalid, N. P. Lalla, and A. V. Pimpale, J. Phys.: Condens. Matter **18**, 10617 (2006).
[56] J. Mastin, M. A. Einarsrud, and T. Grande, Chem. Mater. **18**, 1680 (2006).
[57] A. C. Larson and R. B. V. Dreele, Los Alamos National Laboratory Report No. LAUR 86-748, 2004 (unpublished).
[58] B. H. Toby, J. Appl. Crystallogr. **34**, 210 (2001).
[59] P. F. Peterson, M. Gutmann, T. Proffen, and S. J. L. Billinge, J. Appl. Crystallogr. **33**, 1192 (2000).
[60] Whether or not the system is a ferromagnet or a cluster glass depends on detailed measurements of relaxation effects and whether or not a divergence is observed between ZFC and FC plots of the magnetization versus temperature. For the rest of this paper, we use the term "ferromagnet" to refer to either a conventional ferromagnet or a ferromagnetic cluster glass. See Ref. 36 for a detailed discussion of a ferromagnet versus a cluster glass.
[61] S. Kolesnik, B. Dabrowski, J. Mais, M. Majjiga, O. Chmaissem, A. Baszczuk, and J. D. Jorgensen, Phys. Rev. B **73**, 214440 (2006).
[62] J. F. Mitchell, D. N. Argyriou, C. D. Potter, D. G. Hinks, J. D. Jorgensen, and S. D. Bader, Phys. Rev. B **54**, 6172 (1996).
[63] *Localized to Itinerant Electronic Transition in Perovskite Oxides*, edited by J. B. Goodenough (Springer, Berlin, 2001).
[64] D. Louca, G. H. Kwei, B. Dabrowski, and Z. Bukowski, Phys. Rev. B **60**, 7558 (1999).